

A tunable quantum spin chain with three-body interactions

Khagendra Adhikari* and K. S. D. Beach†

Department of Physics and Astronomy, The University of Mississippi, University, Mississippi 38677, USA

(Dated: December 12, 2021)

We introduce a generalization of the Fredkin spin chain with tunable three-body interactions expressed in terms of conventional spin-half operators. Of the model's two free parameters, one controls the preference for Ising antiferromagnetism and the other controls the strength of quantum fluctuations. In this formulation, the so-called t -deformed model (an exactly solvable, frustration-free Hamiltonian) lives on a unit circle centered on the origin of the phase diagram. The circle demarcates the boundary between ferromagnetic order inside and various antiferromagnetic phases outside. Throughout most of the non-ferromagnetic parts of the phase diagram, the ground state has Dyck word form: i.e., all contributing spin configurations exhibit perfect matching and nesting of spin up and spin down. The exceptions are two regions in which Dyck word mismatches are energetically favorable. We remark that in those regions the energy level spacing can be exponentially small in the system size. It is also the case that exact diagonalization reveals a highly idiosyncratic energy spectrum, presumably because the hard spin twist at the chain ends induces strong incommensurability effects on the bulk system when the chain length is small. As a convergence check, we benchmark our DMRG results to near-double-precision floating-point accuracy against analytical results at exactly solvable points and against exact diagonalization results for small system sizes across the entire parameter space.

I. INTRODUCTION

Quantum spin chains were initially developed as toy models in the early days of quantum mechanics, but by the 1960s they had been realized experimentally in transition metal salts [1–3]. Many other fascinating material examples were subsequently discovered [4–9]. In spite of their simplicity, quantum spin chains exhibit complex properties and behaviors, such as magnetism [10, 11], scale-free criticality [12], quantum phase transitions [13–16], topological order [17, 18], short- and long-range correlations [19], and entanglement [20, 21]. This subject has reached a broader audience following the 2016 Nobel prize, which was awarded in part for Haldane's work to elucidate the topological origin of the divergent behavior of integer- and half-integer-spin chains [22, 23]. Research in this area continues to be spurred by the search for new theoretical insights [24–27] and by the possibility of technological applications in spintronics [28], quantum communication [29, 30], quantum computing [31, 32], quantum simulations [33], and quantum sensors [34].

Frustration-free quantum spin chains with local three-body interactions are relatively recent discoveries, but they have generated great excitement and have already been studied extensively [35–54]. The ground states of the original Motzkin and Fredkin spin chain models are known exactly. Despite being described by a local short-range Hamiltonian, the ground state exhibits robust non-local behavior, including long-distance entanglement [54] and violation of the cluster decomposition property [39]. Furthermore, the entanglement entropy grows as the square root of system size, putting to rest the folk wisdom that a Hamiltonian with local interactions must either obey the area law for a gapped system or deviate by at most logarithmic corrections for the gapless system.

The Fredkin spin chain [53] is a spin-half chain segment subject to three-body correlated-exchange interactions and twisted boundary conditions. Its three-body interactions are structured such that a spin-singlet projector between adjacent spins is operative or not based on the spin state of a neighboring third site. The model is frustration-free, and its ground state (GS) wave function is known to be an equal-weight superposition of all spin configurations of Dyck word form. This is possible because the interactions are in delicate balance. Various models [41, 43, 47, 48, 55] have been proposed that continuously deform the Fredkin model away from this specially tuned point. In Refs. [41, 48], the model is changed to allow for a single tuning parameter that controls the strength and nature of the coupling to the third site. In the two extreme limits, the model reduces to the conventional Heisenberg models with ferromagnetic and antiferromagnetic two-body interactions. A different approach is to modify the two-site projector away from its spin-singlet form, as in Refs. [43, 47]. See the brief review in Appendix A.

The authors of Ref. [43] show that a Fredkin-like model can remain frustration-free while still allowing for an independent tuning parameter at each site that modifies the nature of the local projector (admixing singlet and triplet components). In the uniform case, referred to as the t -deformed Fredkin spin chain [47], an up-down pair of adjacent spins $|\langle\rangle\rangle = |\uparrow\downarrow\rangle$ moves passed its nested third neighbor as per $(\langle\rangle) \Leftrightarrow (\langle\rangle)(\langle\rangle)$ or $(\rangle\rangle) \Leftrightarrow \rangle(\rangle)$. These reconfigurations occur with different probability amplitudes that are functions of the real-valued t . The leftward and rightward motion of short matching pairs is symmetric at the Fredkin point ($t = 1$). The quantum fluctuations freeze out entirely when t approaches 0 or $\pm\infty$; in these extreme limits, the Hamiltonian is semi-classical and the ground state is a pure product state.

The ground state of the t -deformed model is the area-weighted superposition of all Dyck paths. Each weight goes as t^A , where $A \sim \sum_{j=1}^N h_j$ is the area under the spin configuration's height profile, $h_i = \sum_{j=1}^i \sigma_j^z$. The single maximum-area configuration $(((((\cdots))))))$ dominates as $|t| \rightarrow \infty$;

* Electronic address: kadhikar@go.olemiss.edu

† Electronic address: kbeach@olemiss.edu

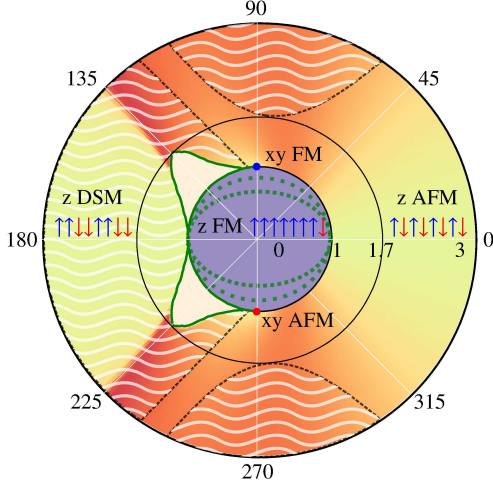


FIG. 1. The diagram shows the various phases of the proposed deformed Fredkin model, plotted in the η - γ plane. The false color background (applied outside the unit circle and outside the two domes) is based on DMRG measurements of dimer order for the $N = 60$ system; the dark red color implies stronger order, following the same scale used in Fig. 6(d). The numerical labels correspond to polar coordinates. Labels at the rim of the outermost circle mark the angle in degrees, and interior labels mark the radii. The patterns of up and down arrows describe the spin states of the classical ground state in the vicinity of the horizontal axis. The text labels denote regions characterized by Ising ferromagnetic order (z FM), Ising antiferromagnetic order (z AFM), doubly staggered Ising magnetic order (z DSM), xy-directed ferromagnetic correlations (xy FM), and xy-directed antiferromagnetic correlations (xy AFM). The relevant order parameters are defined in Sec. IV. The ground state is z FM inside the unit circle, favoring the fully polarized (except the rightmost down spin) state inside the smallest ellipse and stepping down across each dotted green line. Unlike all diagonal measurements, the off-diagonal measurements are antisymmetric about the horizontal diagonal axis. For example, the filled blue circle represents xy-directed FM at the top and the filled red circle denotes xy-directed AFM at the bottom on the unit circle. A distinct hyperbolic region on the left favors fully polarized z DSM. Most parts of the phase diagram comprise of z AFM and dimer order coexisted with dimer order dominating at the top and the bottom parts on the phase diagram. The existence of the unique non-Dyck-form ground state is represented by two domes (Cat's ears like) bounded by a solid green line. Three regions (wavy white: one sector and two hyperbolic planes) enclosed by the dotted black line indicate the first excited state where $S_{\text{tot}}^z(\text{ES}) = 0$ in character. The system is gapped everywhere except green (solid and dotted) lines.

the minimum-area configuration $()() \cdots ()()$ dominates as $t \rightarrow 0$. For $0 < |t| < 1$, the ground state favors Ising antiferromagnetic order (z AFM) and the excitations are gapped. For $1 < |t| < \infty$, the ground state is featureless, and the excitation gap closes exponentially in the system size. Correlations in the easy (xy) plane are either ferromagnetic ($\text{sgn } t = t/|t| = +1$) or antiferromagnetic ($\text{sgn } t = -1$).

We consider a further generalization in terms of two parameters η and γ , such that the t -deformed model lives on the unit circle in the η - γ plane. That is to say, in polar coordinates,

$r^2 = \eta^2 + \gamma^2 = 1$ and $\tan \theta = \gamma/\eta = 2t/(1 - t^2)$. The upper and lower half planes of the phase diagram are connected by symmetry: reflection across the horizontal axis, $\gamma \rightarrow -\gamma$, connects the upper and lower half circles of the t -deformed model according to $t \rightarrow -t$; more generally, this is a transformation that swaps xy ferromagnetic correlations for xy antiferromagnetic by flipping the z direction of every other spin (and also creating an alternation in the sign of the wave function amplitudes that tracks the evenness or oddness of the area under the height field).

The purpose of this paper is to investigate and characterize the new regions at $0 < r < 1$ and $r > 1$. Note that the extended phase diagram is not everywhere frustration-free. We measure the dimer order that coexists with the Ising antiferromagnetism (z AFM) in the original t -deformed model and show how it spreads into the broader phase space. We also identify a regions of doubly staggered Ising magnetic order (z DSM) outside the unit circle and of Ising ferromagnetic order (z FM) inside the unit circle.

We find that our model favors a Dyck-word ground state everywhere that is sufficiently far from the origin ($r \gtrsim 1.7$). The ground state shares the same property closer in, except for two small cat's-ear domes, shown in Fig. 1. We develop a representation of the Hilbert space with spins grouped into pairs whose distinct character is preserved under action by the Hamiltonian we study. To span the full Hilbert space, this representation requires that spin pairs can form conventional (xy-planar), excited (z-canted), and defect (Dyck-word spin mismatch) bonds. We establish that the number of Dyck word defects is a good quantum number and that the ground state within the two domes is of non-Dyck-form with one defect (a single mismatched pair of spins). Unlike the extended quantum critical phases in frustrated systems, which are typically bounded by a line of continuous transitions [56, 57], the transition from Dyck-form to non-Dyck-form here is a simple level crossing.

We organize this paper as follows. The model description and its full Hilbert space are discussed in Secs. II and III, respectively. A detailed discussion of numerical methods is presented in Sec. IV. In Sec. V we analyze the results for various types of ground states in separate subsections. Key findings of the model are summarized in Sec. VI. The model derivation is provided in the Appendix A.

II. MODEL

Our starting point is the Fredkin spin chain [48, 53], a finite chain of N coupled spin-half objects. In the chain's interior, the Hamiltonian

$$H_{\text{bulk}} = \sum_{i=2}^{N-1} H_i \quad (1)$$

is the sum of three-site operators

$$H_i = U_{i-1} P_{i,i+1} + P_{i-1,i} D_{i+1}. \quad (2)$$

Here, $U_i = \frac{1}{2}(\mathbb{1} + \sigma_i^z)$, $D_i = \frac{1}{2}(\mathbb{1} - \sigma_i^z)$, and $P_{i,i+1} = \frac{1}{4}(\mathbb{1} - \sigma_i \cdot \sigma_{i+1})$ are lone-spin-up, lone-spin-down, and spin-singlet projectors, with $\sigma = (\sigma^x, \sigma^y, \sigma^z)$ denoting the Pauli matrices. The projector is directed at two neighboring spins, but it acts only if a third spin on the left (right) is up (down). The boundary term $H_{\text{boundary}} = \alpha_1 D_1 + \alpha_N U_N$ ensures that two strong magnetic fields are applied at the chain's two open ends such that the leftmost (rightmost) spin is almost always up (down). In the numerics presented here, the external field is chosen to be $\alpha_1 = \alpha_N = \alpha = 1000$, which is the largest energy scale in the system by far. The zero-energy frustration-free ground state (GS) of the Fredkin spin chain is in the $S_{\text{tot}}^z(\text{GS}) = 0$ sector while the doubly degenerate excited states (ES) belong to $S_{\text{tot}}^z(\text{ES}) = \pm 1$.

We extend the Fredkin model by replacing the singlet projector $P_{i,j}$ by a more general operator,

$$\tilde{P}_{i,j}(\eta, \gamma) = \frac{1}{4}(\mathbb{1} - \sigma_i^z \sigma_j^z) + \frac{\eta}{4}(\sigma_i^z - \sigma_j^z) - \frac{\gamma}{2}(\sigma_i^+ \sigma_j^- + \sigma_i^- \sigma_j^+), \quad (3)$$

with $2\sigma^\pm = \sigma^x \pm i\sigma^y$ defining the raising and lowering operators. The two independent tuning parameters, η and γ , control the tendency toward Ising antiferromagnetism and the intensity of the quantum fluctuations. The model conventions have been set so that the t -deformed model coincides with $\eta^2 + \gamma^2 = 1$; the position on this circle is defined by $\eta = (1 - t^2)/(1 + t^2)$ and $\gamma = 2t/(1 + t^2)$ [see Eq. (A10) in Appendix A]. The Fredkin point ($t = 1$) is located at $(\eta = 0, \gamma = 1)$, the “north pole” of the unit circle. Note that quantum fluctuations vanish along the horizontal $\gamma = 0$ line. There, the model is governed purely by the energetics, and the ground state is a single, classical configuration.

As a convenience, we transform from Cartesian coordinates to polar coordinates according to $\eta = r \cos \theta$ and $\gamma = r \sin \theta$. Here, $r = 1$ corresponds to a t -deformed model with

$$\cos\left(\frac{\theta}{2}\right) = \frac{1}{\sqrt{1+t^2}}, \quad \sin\left(\frac{\theta}{2}\right) = \frac{t}{\sqrt{1+t^2}}. \quad (4)$$

A unique point ($r = 1, \theta = \pi/2$) represents the Fredkin model. By construction, the ground state energy is positive inside ($r < 1$), negative outside ($r > 1$), and exactly zero on the unit circle. For $r \ll 1$, the model is simply an Ising ferromagnetic, largely independent of angle θ . In the other extreme limit ($r \gg 1$), the ground state is a strong function of the angle θ . At intermediate radii, there is a strong interplay between r and θ , and a rich phase diagram emerges.

III. HILBERT SPACE

A Dyck path of even length $N = 2n$ is a lattice path in the two-dimensional Cartesian plane with traversal from $(0, 0)$ to (n, n) in unit steps—either $(1, 0)$ or $(0, 1)$ —and with the additional constraint that the path never crosses the line $y = x$. In the equivalent landscape picture, the allowed steps are the diagonals $(1, 1)$ or $(1, -1)$, and the path going from $(0, 0)$ to

$(2n, 0)$ never drops below the horizon (the line $y = 0$). The number of unique Dyck paths of length $2n$ is a sequence of numbers called the *Catalan number*. The Catalan number of order n is given by

$$C_n = \frac{1}{n+1} \binom{2n}{n} = \frac{(2n)!}{n!(n+1)!}. \quad (5)$$

The Hamiltonian of the Fredkin spin chain commutes with $S_{\text{tot}}^z (= \sum_{j=1}^N S_j^z)$, and hence the S_{tot}^z is a good quantum number. The set of valid Dyck paths is a subspace within the $S_{\text{tot}}^z = 0$ spin sector of the Hilbert space. The full Hilbert space corresponds to all specifications of spins $\{\sigma_1^z, \sigma_2^z, \dots, \sigma_N^z\}$ executed by a random walk starting from $h_0 = 0$ and ending at h_N . In order to explain the full Hilbert space, we introduce two additional concepts: excitations and defects. There is some flexibility in how one defines these. In this paper, we adopt the convention illustrated in Table I. Each Dyck path

TABLE I. A symbol dictionary translating spin configurations into two alternative representations: viz., height profiles; nested and matched marks of parenthesis.

up spin	down spin	Dyck form	up excitation	down excitation	defect
\uparrow	\downarrow	$\uparrow\downarrow$	$\uparrow\uparrow$	$\downarrow\downarrow$	$\downarrow\uparrow$
\diagup	\diagdown	\diagup	\diagup	\diagdown	\diagdown
$($	$)$	$($	$[$	$]$	$\langle \rangle$

is in 1–1 correspondence with a Dyck word that consists of equal numbers of properly nested left and right parentheses. Although a state in Dyck form or with one or more defects can present in any spin sector, excitations only occur in the $S_{\text{tot}}^z \neq 0$ spin sectors: up excitations in the $S_{\text{tot}}^z > 0$ sectors and down excitations in $S_{\text{tot}}^z < 0$. To ensure a unique representation of the states, we establish the following prescription.

1. Choose $S_{\text{tot}}^z \in \{0, \pm 1, \dots, \pm N/2\}$.
2. Represent all allowed segments of the chain with Dyck-form. The length of the each Dyck-form segment, $L_s \in \{2, 4, \dots, N - 2, N\}$.
3. Represent the excitations,

$$N_e = |S_{\text{tot}}^z| = \begin{cases} 0, & \text{if } S_{\text{tot}}^z = 0 \\ S_{\text{tot}}^z \text{ up-spin pairs from right,} & \text{if } S_{\text{tot}}^z > 0 \\ |S_{\text{tot}}^z| \text{ down-spin pairs from left,} & \text{if } S_{\text{tot}}^z < 0 \end{cases}$$

Unlike the conventional $()$ pairs, excitations themselves cannot be nested; i.e., $[[]]$ is allowed but $[[]]$ is not.

4. Represent the remaining down-up spin pairs as defects. In the presence of excitations in the states, defects can live only to the left (right) of the up (down) excitations.

We define left-cumulative and right-cumulative height functions,

$$h_i = \sum_{j=1}^i \sigma_j \quad \text{and} \quad \bar{h}_i = \sum_{j=i+1}^N \sigma_j, \quad (6)$$

such that $h_0 = 0$ and $h_N = 2S_{\text{tot}}^z$ (whereas $\bar{h}_0 = 2S_{\text{tot}}^z$ and $\bar{h}_N = 0$). The number of defects N_d is defined as

$$N_d = \begin{cases} -\min_i h_i & \text{if } S_{\text{tot}}^z \geq 0, \\ h_N - \min_i h_i = \max_i \bar{h}_i & \text{if } S_{\text{tot}}^z < 0, \end{cases} \quad (7)$$

We have confirmed that the third-site correlated interaction of this two-parameter tunable model has the number of defects N_d as a good quantum number. Hence the reshuffling of short bonds by the Hamiltonian can be used to define a canonical form for each equivalence class of states:

$$\underbrace{(\cdots)}_{N/2-N_d-N_e-1} \underbrace{(\langle \rangle \cdots \langle \rangle)}_{N_d} \underbrace{[\cdots]}_{N_e} () \quad (8)$$

The full Hilbert space for the finite system size $N = 8$ is shown in Fig. 2 using the landscape representation with up-diagonal (\nearrow) and down-diagonal (\searrow). The two lowest-energy states of the two-parameter model in Eq. (3) live in the subspace $(S_{\text{tot}}^z, N_d) \in \{(0, 0), (0, 1), (\pm 1, 0)\}$. Dyck-word form corresponds to $(S_{\text{tot}}^z = 0, N_d = 0)$. For the state with $(S_{\text{tot}}^z = 0, N_d = 1)$ and $(S_{\text{tot}}^z = \pm 1, N_d = 0)$ the state can be represented in terms of a single defect or excitation pair $(\sigma_i, \sigma_j) \in \{[\uparrow], [\downarrow], \langle \rangle\}$ as

$$|N\rangle_{S_{\text{tot}}^z}^{N_d} = \frac{1}{\sqrt{N_{\text{norm}}}} \sum_{\mathcal{D}', \mathcal{D}'', \mathcal{D}'''} g|i, j; \mathcal{D}', \mathcal{D}'', \mathcal{D}'''\rangle, \quad (9)$$

where $|i, j; \mathcal{D}', \mathcal{D}'', \mathcal{D}'''\rangle = |\mathcal{D}'\rangle \otimes |\sigma_i\rangle \otimes |\mathcal{D}''\rangle \otimes |\sigma_j\rangle \otimes |\mathcal{D}'''\rangle$, and $g = g_{ij}(\mathcal{D}', \mathcal{D}'', \mathcal{D}''')$ is the wave function amplitude. Here, the length of Dyck words $\mathcal{D}', \mathcal{D}''$, and \mathcal{D}''' are $i-1$, $j-i-1$, and $N-j$, respectively. The allowed values of (odd) i and (even) j are as follows:

$$\begin{aligned} & \begin{array}{c} [\cdots] \\ \uparrow \\ i \end{array} \quad \begin{array}{c} \uparrow \\ j \end{array} \quad i = 1, 3, \dots, N-3, \\ & \quad \quad \quad j = i+1, i+3, \dots, N-2; \\ & \begin{array}{c} [\cdots] \\ \downarrow \\ i \end{array} \quad \begin{array}{c} \downarrow \\ j \end{array} \quad i = 3, 5, \dots, N-1, \\ & \quad \quad \quad j = i+1, i+3, \dots, N; \\ & \begin{array}{c} \langle \cdots \rangle \\ \downarrow \\ i \end{array} \quad \begin{array}{c} \uparrow \\ j \end{array} \quad i = 3, 5, \dots, N-3, \\ & \quad \quad \quad j = i+1, i+3, \dots, N-2. \end{aligned} \quad (10)$$

The total number of allowed configurations is

$$N^{\text{conf}} = \begin{cases} \frac{5(n-1)(n-2)}{2(n+2)(2n-1)} C_n, & \text{if } S_{\text{tot}}^z = 0, N_d = 1 \\ \frac{2(n-1)}{(n+2)} C_n, & \text{if } S_{\text{tot}}^z = \pm 1, N_d = 0 \end{cases} \quad (11)$$

and $N_{\text{norm}} = \sum_{n=1}^{N^{\text{conf}}} g_n^2$. For example, Eq. (9) takes the form

$$|8\rangle_0^1 = \frac{1}{\sqrt{N_{\text{norm}}}} \left[g_1 |(\cdots) \langle \rangle (\cdots) \rangle + g_2 |(\cdots) \langle \rangle (\cdots) (\cdots) \rangle + g_3 |(\cdots) \langle \rangle (\cdots) (\cdots) \rangle + g_4 |(\cdots) (\cdots) \langle \rangle (\cdots) \rangle + g_5 |(\cdots) (\cdots) \langle \rangle (\cdots) \rangle \right] \quad (12)$$

IV. METHODS

Exact diagonalization (ED) is implemented as described in Ref. [48]. The basis-size reduction due to the discrete symmetries is not enough to significantly reduce the computational cost, so we cannot simulate large systems. To help guide our investigations, however, we have generated the full set of energy eigenstates for $N = 12$ and $N = 16$ over a densely spaced mesh of (r, θ) values.

To access larger sizes, we employ a DMRG algorithm implemented in the open-source C++ library ITensor [58], taking advantage of the fact that S_{tot}^z is a good quantum number in the model. We are mindful of the fact that the high level of entanglement in the vicinity of the Fredkin model and its mirror point at the “south pole” ($r \geq 1$ and $90^\circ \leq \theta \lesssim 110^\circ$ or $250^\circ \lesssim \theta \leq 270^\circ$) requires us to keep many states; farther away, we can be more cavalier about truncating the DMRG basis set. We are also careful about issues of convergence: in and around the two domes of the phase diagram (roughly corresponding to a region $1 \leq r \lesssim 1.2$ and $110^\circ \lesssim \theta \lesssim 260^\circ$) an unexpectedly large number of sweeps is required, because the low-lying energy levels are very closely spaced (see Fig. 3).

Moreover, the convergence is strongly biased by the choice of initial trial state, because the nature of the low-lying states sometimes changes abruptly with a small change in r or θ values. As a workaround, we make a list of possible low energy configurations using ED results for $N \leq 16$. Comparable configurations are then used to seed the DMRG calculations for bigger system sizes. The first excited state belongs to the S_{tot}^z (ES) = 0 spin sector in most parts of this region. So, we calculated the two orthogonal states in $S_{\text{tot}}^z = 0$ having the lowest eigenvalues using many possible trial states. Then, the ground state and the first excited state are found by sorting two lowest energies in the $S_{\text{tot}}^z = 0$ spin sector and the lowest energy in the $S_{\text{tot}}^z = 1$ spin sector.

We have employed a very conservative convergence criterion: the DMRG algorithm runs through $10N$ sweeps using an adaptive truncation cutoff at relative error 10^{-12} with maximum bond dimension $15N$. We have benchmarked our DMRG results to near double-precision floating-point accuracy against ED results for $N \leq 16$. The DMRG computation is carried out for all lattice sizes that are multiples of 4 up to $N = 60$, over a tight mesh of tuning parameter values $r = 0, 0.025, \dots, 2.975, 3$ and $\theta = 0^\circ, 1^\circ, \dots, 359^\circ, 360^\circ$. The most expensive of those simulations corresponds to 600 sweeps with a maximum bond dimension of 900. Various physical quantities are computed in the ground state as a function of the tuning parameters r, θ ; i.e., $O(r, \theta) = \langle \hat{O} \rangle =$

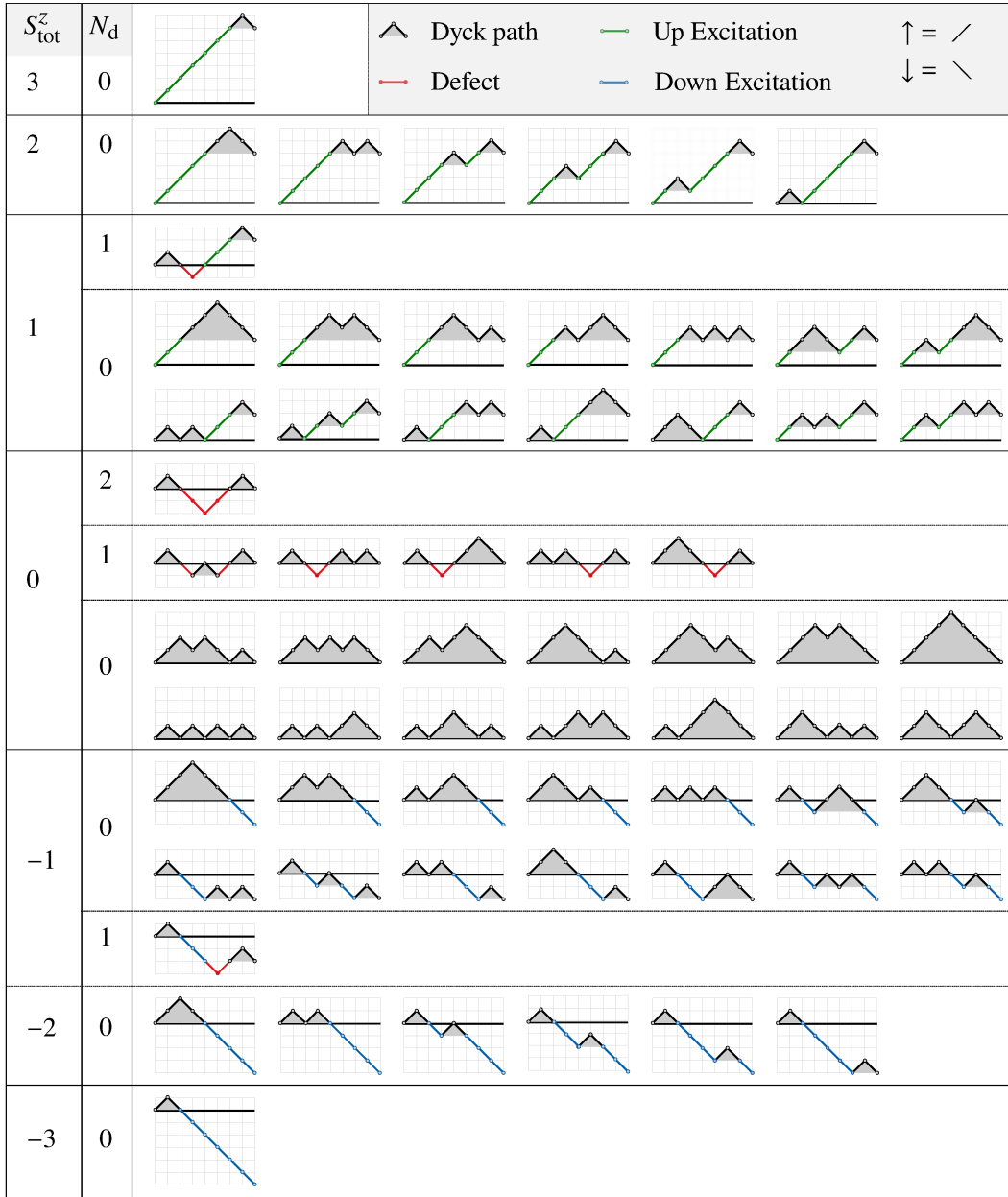


FIG. 2. Full Hilbert space for $N = 8$ with infinite twisted boundary conditions. The horizontal lines separate the different blocks of subspace having definite quantum numbers: the total spin in z -direction, S_{tot}^z , and number of defects, N_d .

$\langle \psi_0(r, \theta) | \hat{O} | \psi_0(r, \theta) \rangle$. These include the spin profile $\langle \sigma_i^z \rangle$, dimer profile $\langle \sigma_i^z \sigma_{i+1}^z \rangle - \langle \sigma_i^z \rangle \langle \sigma_{i+1}^z \rangle$, dimer order parameter

$$\langle d_{\parallel} \rangle = \frac{1}{N} \sum_{j=1}^{N-1} c_j [\langle \sigma_j^z \sigma_{j+1}^z \rangle - \langle \sigma_j^z \rangle \langle \sigma_{j+1}^z \rangle] \quad (13)$$

where

$$c_j = (-1)^j \begin{cases} 1/2, & \text{if } j = 1 \text{ or } N \\ 1, & \text{otherwise} \end{cases}$$

Ising ferromagnetic order parameter (z FM)

$$\langle m_{\parallel}(\text{FM}) \rangle = \frac{1}{N} \sum_{j=1}^N \langle \sigma_j^z \rangle, \quad (14)$$

Ising antiferromagnetic order parameter (z AFM)

$$\langle m_{\parallel}(\text{AFM}) \rangle = \frac{1}{N} \sum_{j=1}^N (-1)^j \langle \sigma_j^z \rangle, \quad (15)$$

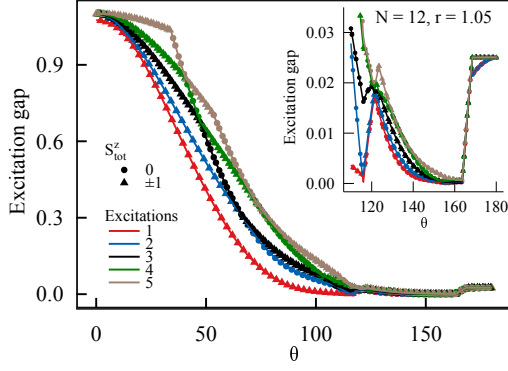


FIG. 3. (Color online) Exact diagonalization gap-spectrum results for $r = 1.05$ and $N = 12$. Few low-lying energy spectra belong to $|S_{\text{tot}}^z| \leq 1$ sector and it shows how difficult it is to integrate out the ground state and first excited state energy in the non-Dyck-form dome (see the north-west quadrant of Fig. 1) because the spacing between them is narrow. The first excited state (red line) make a transition from $S_{\text{tot}}^z(\text{ES}) = 1$ (solid triangle) to $S_{\text{tot}}^z(\text{ES}) = 0$ (solid circle) just before entering the non-Dyck-form ground state from the left at angle $\theta = 115.5^\circ$ as shown in the inset.

doubly staggered Ising magnetic order parameter (z DSM)

$$\langle m_{\parallel}(\text{DSM}) \rangle = \frac{1}{N} \sum_{j=1}^N c_j \langle \sigma_j^z \rangle \quad (16)$$

where

$$c_j = \begin{cases} +1, & \text{if } j = 0, 1 \pmod{4} \\ -1, & \text{if } j = 2, 3 \pmod{4} \end{cases}$$

the xy-plane ferromagnetic order parameter (xy FM)

$$\langle m_{\perp}^2(\text{xy FM}) \rangle = \frac{1}{N^2} \sum_{i,j=1}^N \langle \sigma_i^+ \sigma_j^- + \sigma_i^- \sigma_j^+ \rangle, \quad (17)$$

and the xy-plane antiferromagnetic order parameter (xy AFM)

$$\langle m_{\perp}^2(\text{xy AFM}) \rangle = \frac{1}{N^2} \sum_{i,j=1}^N (-1)^{i+j} \langle \sigma_i^+ \sigma_j^- + \sigma_i^- \sigma_j^+ \rangle. \quad (18)$$

V. RESULTS AND DISCUSSION

Unlike the upper half-plane where wave function amplitudes are all positive, the wave function amplitudes in the lower circular plane contain an admixture of positive and negative signs. About the horizontal line ($\gamma = 0$), diagonal (σ^z dependent only) and off-diagonal (products of σ^+ and σ^-) measurements are symmetric and anti-symmetric, respectively. For example, xy FM and xy AFM measurements in Fig. 6(b) have peaks at $(r, \theta) = (1, 90^\circ)$ and $(1, 270^\circ)$, respectively. So, we discuss our diagonal measurement results only for the upper semi-circular

plane, and a similar explanation applies to the lower semi-circular plane. We analyze the ground state properties of the system at distinct regions of the phase space separately in the Secs. V A–V D.

A. Fluctuation-free limit ($\gamma = 0$)

The classical energy of Eq. (2) is given by

$$E(\eta, \gamma = 0)_i = \begin{cases} (1 + \eta)/2, & \text{if } |(()) \rangle \text{ or } |() () \rangle \\ (1 - \eta)/2, & \text{if } |() () \rangle \text{ or } |() () \rangle \\ 0, & \text{otherwise} \end{cases} \quad (19)$$

The energy difference ($\Delta E_i = \pm \eta$) in Eq. (19) can be viewed as a movement of a short bond $()$ to the left or right; i.e., $(() \Leftrightarrow () () \text{ or } () \Leftrightarrow () ()$. In Table II, we summarize a list of several low-lying energy configurations of the classical model using Eq. (19). The lowest two energy configurations

TABLE II. (Color online) A list of relevant spin configurations for the two low-lying states of the classical model of size $N = 8$.

State	Configurations	$E(N, \eta, \gamma = 0, h)$
[1] (z FM)	$ \overline{\uparrow} \overline{\uparrow} \overline{\uparrow} \overline{\uparrow} () \rangle$ $ () \underline{\downarrow} \underline{\downarrow} \underline{\downarrow} \underline{\downarrow} \rangle$	$(1 + \eta)/2$
[2]	$ () \overline{\uparrow} \overline{\uparrow} () \rangle$ $ () \underline{\downarrow} \underline{\downarrow} () \rangle$	1
[3] (z AFM)	$ () () () () \rangle$	$(N - 2)(1 - \eta)/2$
[4]	$ \overline{\uparrow} \overline{\uparrow} () () \rangle$ $ () () \underline{\downarrow} \underline{\downarrow} \rangle$	$(N - 4)(1 - \eta)/2 + (1 + \eta)/2$
[5] (D-Wall)	$ (((())))) \rangle$	$1 + \eta$
[6] (z DSM)	$ (()) (()) \rangle$	$N(1 + \eta)/4$ $N = 0 \pmod{4}$
[7]	$ () () () () \rangle$ $ (()) \overline{\uparrow} () \rangle$ or others	$(N - 2)(1 + \eta)/4$ $N = 0 \pmod{4}$
[8]	$ () () () \overline{\uparrow} \rangle$ $ \underline{\downarrow} \underline{\downarrow} () () () \rangle$	$(N - 3)(1 - \eta)/2 + \alpha$
[9]	$ \langle () () () \rangle \rangle$	$(N - 2)(1 - \eta)/2 + 2\alpha$

of this classical model are discussed in Secs. V A and V A.

On the positive x-axis ($\theta = 0, \eta = r$)

The ground state, excited state, and the excitation gap are shown in Table III. Let us define two critical radii $r_c(N) = (N - 4)/(N - 2)$ and $r_{cc}(N) = (N - 3)/(N - 1)$. At $r = 0$, only the first term survives in Eq. (3). The ground state favors the doubly

TABLE III. The table summarizes the ground state, first excited state, and the excitation gap at $\theta = 0^\circ$. The corresponding spin configuration of the state (GS or ES) are shown in Table II.

Radius	GS⟩	ES⟩	$\Delta(N, r, \alpha)$
$r = 0$	$ 1\rangle$	$ 2\rangle, 5\rangle$ or others	$1/2$
$0 < r < r_c(N)$	$ 1\rangle$	$ 2\rangle$	$(1 - r)/2$
$r_c(N) < r < r_{cc}(N)$	$ 1\rangle$	$ 3\rangle$	$(N - 1)(1 - r)/2 - 1$
$r_{cc}(N) < r < 1$	$ 3\rangle$	$ 1\rangle$	$1 - (N - 1)(1 - r)/2$
$r = 1$	$ 3\rangle$	$ 4\rangle$ or others	$r + (r - 1)/2$
$1 < r < \alpha$	$ 3\rangle$	$ 4\rangle$	$r + (r - 1)/2$
$r = \alpha$	$ 3\rangle$	$ 4\rangle, 8\rangle$	$\alpha + (r - 1)/2$
$\alpha < r < 2\alpha + 1$	$ 3\rangle$	$ 8\rangle$	$\alpha + (r - 1)/2$
$r = 2\alpha + 1$	$ 3\rangle$	$ 8\rangle, 9\rangle$	2α
$r > 2\alpha + 1$	$ 3\rangle$	$ 9\rangle$	2α

degenerate z FM state and the first excited state belongs to the highly degenerate states of types $|2\rangle$ and $|5\rangle$ with an excitation gap $\Delta = 1/2$. For a finite system size N , the first-order phase transition from z FM to z AFM occurs exactly at $r_{cc}(N)$. In the thermodynamic limit, the phase transition occurs exactly at $r_{cc}(N \rightarrow \infty) = 1$. Both z FM and z AFM are fully polarized at this angle and they belong to the $S_{\text{tot}}^z(\text{GS}) = (N - 2)/2$ and $S_{\text{tot}}^z(\text{GS}) = 0$, respectively. For $r \geq 1$, the ground state favors z AFM. The excitation gap is $\Delta(\text{z FM}) = (1 - r)/2$ for $r < 1$, and $\Delta(\text{z AFM}) = r + (r - 1)/2$ for $r \geq 1$ in the limit $\alpha \rightarrow \infty$.

The ground state is independent of the field strength α (tested for $\alpha \geq 1$). However, the magnitude of field strength affects the measurement of the excitation gap if $r \geq \alpha$ and the angle θ is small. The spin-flip at the boundary adds extra energy α to the system resulting $S_{\text{tot}}^z(\text{ES}) = 0$ excitation in stead of $S_{\text{tot}}^z(\text{ES}) = 1$. At exactly $r = \alpha$, the state $|8\rangle$ with the excitation gap $\Delta(r, \alpha) = \alpha + (r - 1)/2$ is equal to the state $|4\rangle$. So, the state $|8\rangle$ is the excited state in the range $\alpha < r < 2\alpha + 1$. At exactly $r = 2\alpha + 1$, the state $|9\rangle$ with two spins flips at the boundary overlap with previous doubly degenerate excited states giving common gap $\Delta(\alpha) = 2\alpha$. For $r > \alpha$, a unique state $|9\rangle$ with a constant gap $\Delta(\alpha) = 2\alpha$ is the excited state.

On the negative x-axis ($\theta = 180^\circ$, $\eta = -r$)

The ground state, excited state, and the excitation gap are shown in Table IV. For $0 < r < 1$, the ground state is the doubly degenerate z FM, and the first excited state is highly degenerate. At $r = 1$, the z AFM is highly penalized, but all other states including the domain wall (D-Wall) have the same energy resulting in highly degenerate ground states with $S_{\text{tot}}^z(\text{GS}) = 0, \pm 1, \dots, \pm(N - 2)/2$. The highly degenerate excited state

TABLE IV. (color online) The table summarizes the ground state, excited state, and the excitation gap at $\theta = 180^\circ$. The corresponding spin configurations of the state (GS or ES) are shown in Table II.

Radius	GS⟩	ES⟩	$\Delta(N, r)$
$r = 0$	$ 1\rangle$	$ 2\rangle, 5\rangle$ or others	$1/2$
$0 < r < 1$	$ 1\rangle$	$ 5\rangle$ $ (\rangle \langle \rangle \rangle \langle \rangle \rangle$ $ [\rangle \rangle \langle \rangle \rangle \rangle$ or others	$(1 - r)/2$
$r = 1$	$ 5\rangle$ or others	$ 2\rangle$ $ [\rangle \rangle \rangle \rangle \rangle$ $ (\rangle \langle \rangle \rangle \rangle \rangle$ or others	1
$1 < r < \infty$	$ 6\rangle$	$ 7\rangle$	$(r - 1)/2$

belongs to different sectors $S_{\text{tot}}^z = 0, \pm 1, \dots, \pm(N - 4)/2$. For $1 < r < \infty$ and $N = 0 \pmod{4}$, the ground favors a state that forms a repeated patterns of four spins, z DSM. The degenerate excited states belong to $S_{\text{tot}}^z(\text{ES}) = 0, 1$ sectors. The excitation gap is independent of the system size. The $N = 2 \pmod{4}$ sizes are excluded from this work to avoid ambiguity because their ground state is degenerate in the range $1 < r < \infty$. For example, $E(N, \eta) = (N - 2)(1 + \eta)/4$ for $|(\rangle \langle \rangle \rangle \rangle$, $|[\rangle \rangle \langle \rangle \rangle \rangle$, and many other states.

B. Unit circle ($r = 1$)

On the unit circle, the ground state is the area-weighted sum of the Dyck-form. The zero-energy unique ground state belongs to $S_{\text{tot}}^z(\text{GS}) = 0$, but the excitations are doubly degenerate in $S_{\text{tot}}^z(\text{ES}) = \pm 1$ spin sectors. The left unit semi-circle is featureless (no order), and the excitation gap vanishes exponentially fast. On the right unit semi-circle, the ground state is ordered, and the excitations are gapped. The spectral gap obeys the threshold criteria for frustration-free spin systems with boundary [59]. The peaks of z AFM ($= \cos \theta/2$) and the excitation gap at $(r, \theta) = (1, 0^\circ)$ both vanish smoothly at the Fredkin point $(1, 90^\circ)$. There is a strong dimer order at $(1, \approx 65^\circ)$ that gradually weakens with changing angle until it disappears completely at $(1, 0^\circ)$ and $(1, 90^\circ)$. For finite system sizes, the xy FM is smeared out in the vicinity of the Fredkin point, but it collapses to a delta function in the thermodynamic limit. Although diagonal measurements are symmetric about the horizontal line ($\gamma = 0$), off-diagonal measurements are antisymmetric. So, strong xy AFM is measured at the bottom of the unit circle that was not included in the origin t -deformed model.

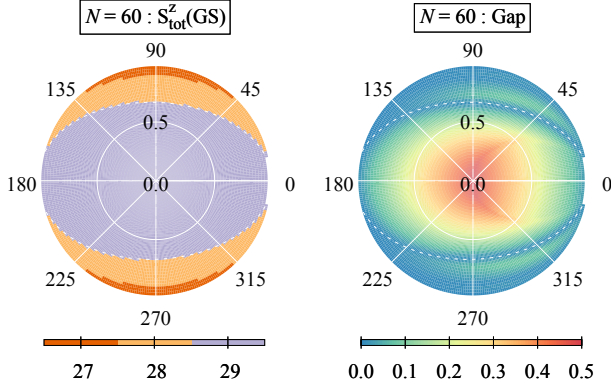


FIG. 4. (Color online) The discrete colormap for $N = 60$ and $r < 1$: the inner label represents the radii, and the outer circular label denotes the angles. The data in the vicinity of ($r = 1, \theta = 0$) are not shown to exclude the finite size effect. Left: Three different colors denote the ground state spin sectors $S_{\text{tot}}^z(\text{GS}) = (N - 2)/2$, $(N - 4)/2$, and $(N - 6)/2$ for the innermost, middle, and the outermost elliptical regions, respectively. The ferromagnetic order weakens along the vertical diagonal away from the center. Right: The excitation gap is $\Delta = 1/2$ at the center and vanishes as $r \rightarrow 1$. The gapless elliptical boundaries correspond to the spin sector crossover in the ground state as shown in Fig. 4 (Left).

C. Inside the unit circle ($r < 1$)

For $\theta = 180^\circ$, the phase transition from z FM to D-Wall state occurs exactly at $r = 1$, independent of the system size. However, for $\theta = 0$, the phase transition from z FM to z AFM occurs exactly at $r_{\text{cc}}(N)$ for a finite system size, N . For $r_{\text{cc}}(N) < r < 1$, true nature of the system in the ground state is suppressed by the finite size effect where ground state favors z AFM only for the finite system. Although the ground state properties are independent of system size for $r \leq r_{\text{cc}}(N)$, the excitation gap does only for $r \leq r_c(N)$. In the thermodynamic limit, $r_c(\infty) \rightarrow r_{\text{cc}}(\infty) \rightarrow 1$. In Fig. 4, we omitted the data in the vicinity of ($r \lesssim 1, \theta \approx 0$) to exclude the finite-size effect. Along the vertical line ($\eta = 0$) in the phase diagram, the ground state belongs to $S_{\text{tot}}^z(\text{GS}) = (N - 2)/2$ sectors for $0 \leq r \lesssim 2/3$. As r increases, the spin sector decreases gradually first and then exponentially fast as ($r \lesssim 1, \theta = 90^\circ$) resulting in $S_{\text{tot}}^z(\text{GS}) = 0$ at Fredkin point. The model is gapped at the center, $\Delta(r = 0) = 1/2$, and gapless along the unit circle. The ellipses with gapless boundary correspond to the ground state level crossing in the spin sectors $S_{\text{tot}}^z(\text{GS})$: $(N - 2)/2 \rightarrow (N - 4)/2$, $(N - 4)/2 \rightarrow (N - 6)/2$, and so on as shown in Fig. 4. The ground state and the excited state belong to different spin sectors and satisfy $S_{\text{tot}}^z(\text{GS}) = S_{\text{tot}}^z(\text{ES}) \pm 1$ (– in transition window followed by the gapless boundary and + elsewhere). There is no quantum-fluctuation in $S_{\text{tot}}^z(\text{GS}) = (N - 2)/2$ sector because promoting the N^{th} down spin to up costs an additional energy h to the system. So, the ground state energy is $E_0 = (1 + \eta)/2$ (independent of γ) with the unique z FM inside the innermost ellipse shown in Fig. 4.

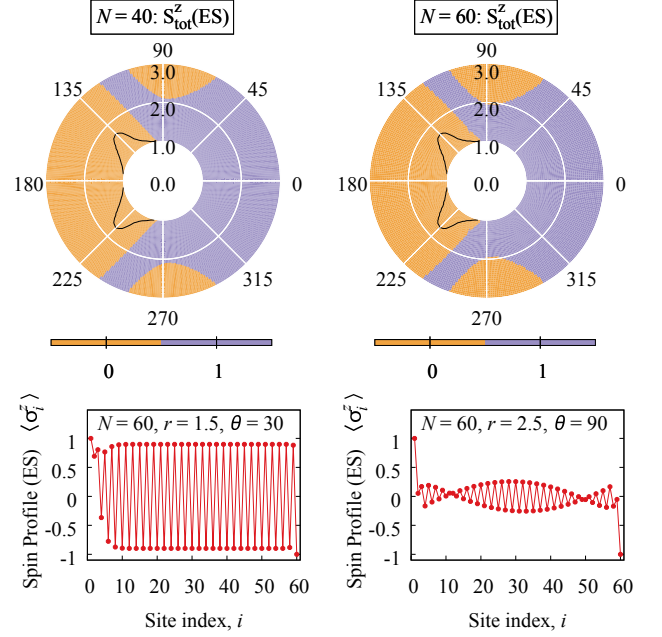


FIG. 5. (Color online) Top: The colormap denotes the discrete values of $S_{\text{tot}}^z(\text{ES})$ measured in the first excited state, and also shows the expansion of hyperbolic regions towards the center with the increasing system size, N . The excitation $S_{\text{tot}}^z(\text{ES})$ changes while approaching the non-Dyck-form ground state phase (area enclosed by the solid black line). Bottom: Spin profile measured in the excited state for a finite size $N = 60$ at points ($r = 1.5, \theta = 30^\circ$) and ($r = 2.5, \theta = 90^\circ$) showing the distinct profiles for two types of excitations.

D. Outside the unit circle ($r > 1$)

The ground state is Dyck-form everywhere except in two Cat ears like plane domes residing on the left semi-circular plane of the phase space (see Figs. 5,6). The non-Dyck-form and Dyck-form ground states are discussed in Secs. VD and VD, respectively.

Non-Dyck-form ground state

The non-Dyck-form unique ground state is observed for $N \geq 10$ in the dome residing its base along the unit circle and peaked at ($r \approx 1.7, \theta \approx 135^\circ$) as shown in Fig. 6. The ground state shows idiosyncratic nature while making phase transition from z AFM at angle 0° through z DSM order at angle 180° by creating different numbers of peaks in the spin profile as shown in Fig. 7 (Top). The nature of forming a group of spins cluster and transition between them make the system strongly size-dependent non-Dyck-form ground state. The Dyck-form and non-Dyck-form do not co-exist in a particular state because they have distinct quantum numbers (see Sec. III). In two domes, the ground state favors $S_{\text{tot}}^z = 0$ and $N_d = 1$. The first excited state heavily depends on (r, θ) values and belongs to $(S_{\text{tot}}^z, N_d) \in \{(0, 0), (0, 1)\}$ subspace of the Hilbert space. Since the states are not entangled, DMRG should work perfectly but this is not the case. The small energy scale (see Fig. 3) hinders

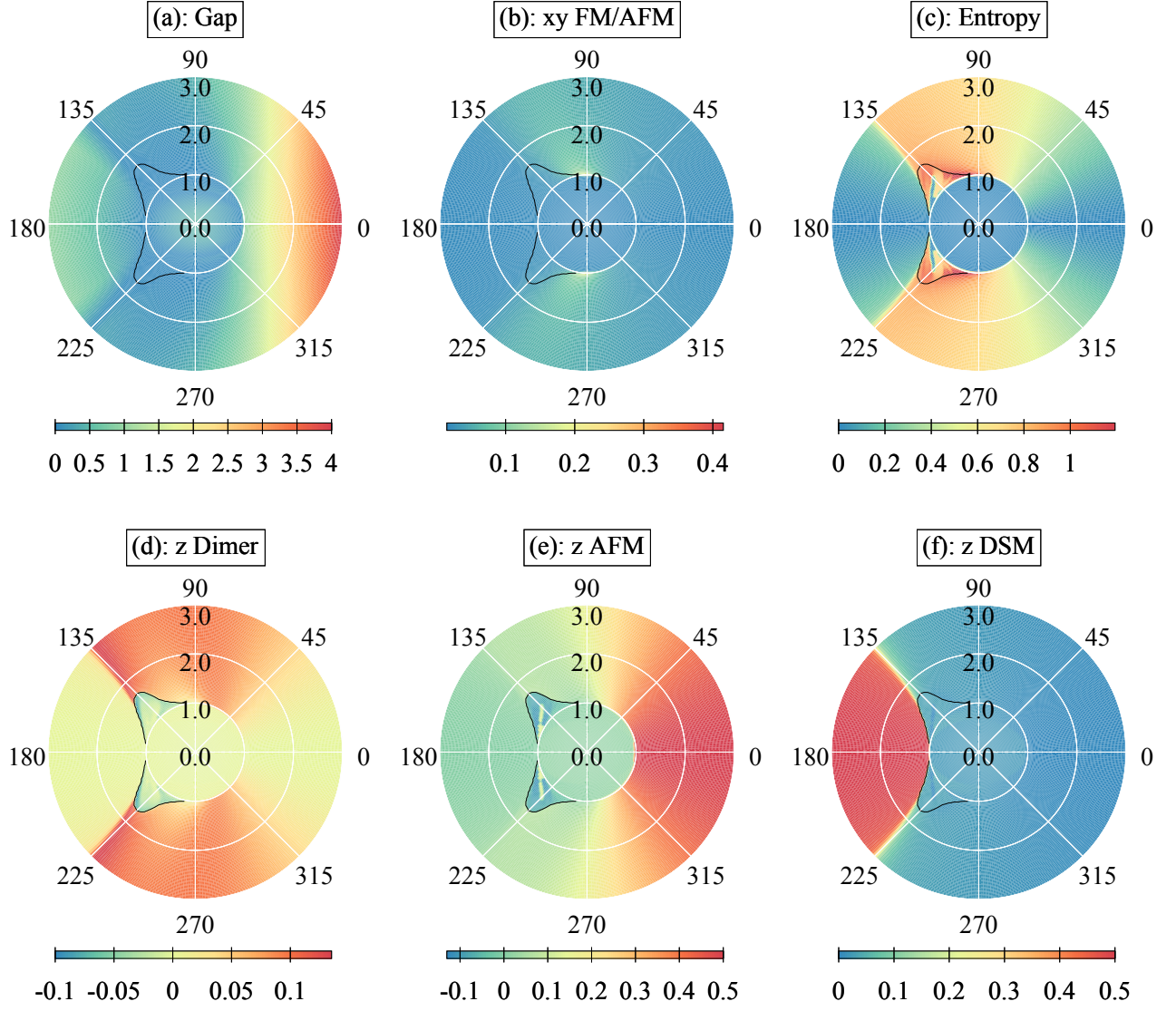


FIG. 6. (Color online) Sample color maps for the finite system $N = 60$ where black solid line represent the domes boundaries. (a) Excitation gap. (b) The xy -directed FM (AFM) on the upper (lower) semi-circular regions. (c) The von Neumann entanglement entropy. (d) The dimer order parameter showing slightly varying magnitudes at different parts of the phase diagram. (e) The Ising anti-ferromagnetic order parameter, z AFM. (f) Doubly staggered Ising magnetic order parameter, z DSM.

to find the global minima, and the solution is also biased to the initial trial state (noise observed in the domes). In some parts of the non-Dyck-form ground state, the lowest-lying energy states are almost continuum where Dyck-form ground state appears for few selected system sizes and special tuning points as a coincidence (spin profile shown in Fig. 7 (Bottom) and line observed in Fig. 6 (c and e) in the domes). Additionally, the strong size-dependent nature observed in the measured values makes extrapolation almost impossible (see Fig. 3). We believe that this non-Dyck-form dome appears because of frustration arising from many competing phases surrounding it. The size of the dome is robust and already conversed for $N = 60$ as tested against $N = 120$.

Dyck-form ground state

The unique ground state is in $S_{\text{tot}}^z(\text{GS}) = 0$ sector everywhere, and the first excitation belongs to $S_{\text{tot}}^z(\text{ES}) = 0, \pm 1$ as shown in Fig. 5 (Top). The hyperbolic regions containing Dyck-form ($S_{\text{tot}}^z(\text{ES}) = 0, N_d = 0$) excitation emerges for $N \geq 10$ and broaden with the increasing system size. As a result, the vertex approaches ($r \approx 1.7, \theta \lesssim 90^\circ$; peak of the non-Dyck-form dome) in the thermodynamic limit. Unlike $S_{\text{tot}}^z(\text{ES}) = 1$ excitation where the spin-flip occurs at one end of the chain, even the number of spins flip resulting in the Dyck-form excitation as shown in Fig. 5 (Bottom).

The excitation is gapless only along the unit circle and the boundary of non-Dyck-form, leaving the system gapped every-

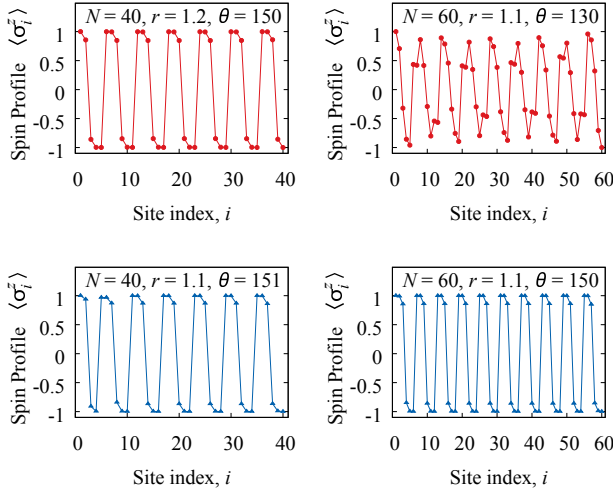


FIG. 7. (Color online) Top: The sample spin profiles showing non-Dyck-form ground states in the dome. The configuration $((())\langle(((())\dots((()))\rangle((())$ and $((())\langle(((())\dots((()))\rangle((())$ represent sample configurations of the average spin profile on the top left and top right, respectively. The red angle brackets in the spin configurations denote a single defect in the spin profile. Bottom: Spin profiles showing the potential of forming Dyck-form ground states in a small region of phase space inside the dome. The average spin profiles on the bottom left and bottom right panel are $((())((()))\dots((()))$, and $((()))\dots((()))$ respectively.

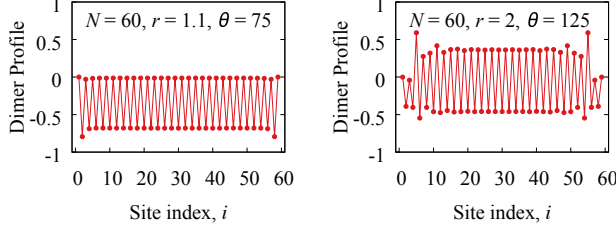


FIG. 8. (Color online) Dimer profile measured in the ground state for a finite size $N = 60$ at two points ($r = 1.5, \theta = 75$) and ($r = 2, \theta = 125$) representing distinct dimer patterns.

where on the phase space. The excitation gap increases along the radial direction away from the center for all angles. In the angular direction, the gap maximum at $\theta = 0^\circ$ decreases gradually and attains its minima at the hyperbolic boundary on the left semi-circular region. In z DSM, the region enclosed by the hyperbolic boundary, the excitation gap does not vary much with the change in angle θ .

The xy-directed ferromagnetic correlation observed at the Fredkin point appears to leak away from the center on the left side of the vertical line as shown in Fig. 6 (b). Although von Neumann entropy shows a significant boost in that region, it does not scale with the system size because the system is gapped and follows the area law of entanglement entropy. Unfortunately, this apparent entangled state requires a larger bond dimension in DMRG calculation resulting in additional time

complexity.

The fully saturated z AFM at $\theta = 0^\circ$ decreases continuously in the angular direction until it completely vanishes at the z DSM boundary as shown in Fig. 6(e). In the radial direction away from the center, z AFM first increases gradually, and then saturates to a finite value. The dimer order is absent in both z DSM and strong z AFM regions. The dimer order peak at ($r = 1, \theta \approx 65^\circ$) shifts toward the left part of the phase space with the increasing value of radius r as can be seen in Fig. 6(d). The slightly different magnitude of dimer order observed in Fig. 6(d) are shown by the distinct dimer profiles in Fig. 8.

VI. CONCLUSIONS

In Sec. III, we discussed how to represent the Hilbert space using the language of matching and nested spin pairs. Conventional pairs, with a spin up to the left and spin down to the right, are the building blocks of the Dyck-word ground state. By promoting certain conventional bonds to a bond of different character—either an excited bond that cants the spin state out of the xy plane or a defect bond that carries a Dyck word mismatch—we were able to cover the entire Hilbert space. We derived formulas relating the number of excited and defect bonds to the explicit spin arrangement in a given state, and we offered a detailed prescription for converting from the raw spin representation into the bond representation. Most important, we argued that the population count for each kind of bond is a good quantum number for the model Hamiltonian considered in Sec. II.

Figure 1 shows a summary of the zero-temperature quantum phase diagram, based on an extrapolation of various numerical measurements on finite-size systems to the thermodynamic limit. The diagonal measurements (those involving σ^z only) are symmetric about the horizontal ($\gamma = 0$) axis, whereas off-diagonal measurements (involving σ^+ and σ^-) are antisymmetric. The two-parameter extended model we have proposed is exactly solvable on the horizontal line ($\gamma = 0$) and on the unit circle ($\eta^2 + \gamma^2 = 1$). For $r < 1$, the ferromagnetic ground state is doubly degenerate. For $r \geq 1$, the ground state is everywhere unique—except at the point ($r = 1, \theta = 180^\circ$)—for all system sizes satisfying $N = 0 \pmod{4}$. Along the line ($r > 1, \theta = 180^\circ$), the ground state is highly degenerate for sizes $N = 2 \pmod{4}$, since the desired doubly staggered pattern is prevented from forming; hence, these sizes are excluded.

The t -deformed model lies on the unit circle, and the line $\eta = 0$ separates the gapped, ordered phases on the right from the gapless, disordered phases on the left. The latter belong to a region in which the excitation gap closes exponentially fast. That unit circle also demarcates a boundary between regions that show ferromagnetic behavior inside and coexistence of antiferromagnetic and dimerized behavior elsewhere. The dimer order is strong in the upper and lower parts of the diagram, where quantum fluctuations are enhanced. On the other hand, the right part of the phase space favors z AFM behavior and the left supports z DSM behavior. The system is gapped everywhere except on ellipses inside the unit circle and on the

boundary of the domes on the left part of the phase diagram. Most parts of the phase space favor the Fredkin-like Dyck-form ground state except the two domes and inside the unit circle. The two domes on the left and the Dyck-form ($S_{\text{tot}}^z = 0, N_d = 0$) excitation on the top of the phase diagram both emerge only for $N \geq 10$; in the thermodynamic limit, they all touch the circle at $r \approx 1.7$, approaching it from opposite sides. Inside the two domes, the ground state favors $S_{\text{tot}}^z = 0$ and $N_d = 1$, leaving Dyck-form to the higher energy state. Inside the unit circle, the ground state is ferromagnetic (higher $|S_{\text{tot}}^z|$) with no defects ($N_d = 0$).

The tunable Hamiltonian we have proposed and studied in this paper puts the Fredkin model and its t -deformed generalization in the context of a larger space of models that have a well-defined notion of conventional, excited, and defect bonds. This is interesting because the identification of the bond character relies on knowledge of the complete spin configuration; in other words it is a global rather than local property of the spin state and hence has a topological nature. Our work makes clear that, even though the t -deformation is frustration free, its quantum-disordered ground state is nonetheless a result of a special tuning of the competing interactions, one that carefully balances their ferromagnetic and antiferromagnetic tendencies.

Appendix A: Generalization of the t -deformed model

We consider the colorless $S = 1/2$ specialization of the frustration-free, t -deformed Fredkin spin chain described in Ref. [43]. The Hamiltonian

$$H(t) = H_F(t) + H_{\text{boundary}} \quad (\text{A1})$$

is the sum of bulk and boundary terms,

$$H_F(t) = \sum_{j=2}^{N-1} (|\phi_j^A\rangle\langle\phi_j^A| + |\phi_j^B\rangle\langle\phi_j^B|) \quad (\text{A2})$$

and

$$H_{\text{boundary}} = |\downarrow_1\rangle\langle\downarrow_1| + |\uparrow_N\rangle\langle\uparrow_N|. \quad (\text{A3})$$

The operators in H_F project onto the states

$$|\phi_j^A\rangle = \frac{1}{\sqrt{1 + |t_j^A|^2}} \left[|\uparrow_{j-1}\uparrow_j\downarrow_{j+1}\rangle - t_j^A |\uparrow_{j-1}\downarrow_j\uparrow_{j+1}\rangle \right] \quad (\text{A4})$$

and

$$|\phi_j^B\rangle = \frac{1}{\sqrt{1 + |t_j^B|^2}} \left[|\uparrow_{j-1}\downarrow_j\downarrow_{j+1}\rangle - t_j^B |\downarrow_{j-1}\uparrow_j\downarrow_{j+1}\rangle \right]. \quad (\text{A5})$$

The unspecified parameters satisfy $t_j^B = t_{j-1}^A$. If we treat them all on an equal footing, as in Ref. [47], then the model depends on a single, site-independent parameter $t = t_j^A = t_j^B$.

The projector in Eq. (2) can be represented as

$$P_{i,j} = |S_{i,j}\rangle\langle S_{i,j}|, \quad (\text{A6})$$

where

$$|S_{i,j}\rangle = \frac{1}{\sqrt{2}} \left[|\uparrow_i\downarrow_j\rangle - |\downarrow_i\uparrow_j\rangle \right] \quad (\text{A7})$$

is the singlet formed by spin at sites i and j . The multi-parameter generalization [43] of this state takes the form

$$|S(t)_{i,j}\rangle = \frac{1}{\sqrt{1 + t_{ij}^2}} \left[|\uparrow_i\downarrow_j\rangle - t_{ij} |\downarrow_i\uparrow_j\rangle \right], \quad (\text{A8})$$

which is properly normalized and allows for admixing of the various spin-triplet components. The model preserves the frustration-free nature of original Fredkin model in the sense that the ground state minimizes each term in the Hamiltonian individually.

For simplicity, we work on single-tuning-parameter t -deformation studied in Ref. [47],

$$|S(t)_{i,j}\rangle = \frac{1}{\sqrt{1 + t^2}} \left[|\uparrow_i\downarrow_j\rangle - t |\downarrow_i\uparrow_j\rangle \right], \quad (\text{A9})$$

from which the usual Fredkin model is recovered at $t = 1$. The t -deformed ground consists of a sum of Dyck-form spin states whose weight is proportional to area under the corresponding height profile. Let us express the spin-singlet projector in terms of Pauli matrices, with $2\sigma^\pm = \sigma^x \pm i\sigma^y$ defining the raising and lowering operators.

$$\begin{aligned}
P(t)_{i,j} &= |S(t)_{i,j}\rangle \langle S(t)_{i,j}| \\
&= \frac{1}{1+t^2} [(|\uparrow_i \downarrow_j\rangle - t|\downarrow_i \uparrow_j\rangle) (\langle \uparrow_i \downarrow_j| - t \langle \downarrow_i \uparrow_j|)] \\
&= \frac{1}{1+t^2} [|\uparrow_i \downarrow_j\rangle \langle \uparrow_i \downarrow_j| + t^2 |\downarrow_i \uparrow_j\rangle \langle \downarrow_i \uparrow_j| - t (|\uparrow_i \downarrow_j\rangle \langle \downarrow_i \uparrow_j| + |\downarrow_i \uparrow_j\rangle \langle \uparrow_i \downarrow_j|)] \\
&= \frac{1}{1+t^2} \left[\frac{1}{4} (\mathbb{1} + \sigma_i^z) (\mathbb{1} - \sigma_j^z) + \frac{t^2}{4} (\mathbb{1} - \sigma_i^z) (\mathbb{1} + \sigma_j^z) - t (\sigma_i^+ \sigma_j^- + \sigma_i^- \sigma_j^+) \right] \\
&= \frac{1}{1+t^2} \left[\frac{1+t^2}{4} (\mathbb{1} - \sigma_i^z \sigma_j^z) + \frac{1-t^2}{4} (\sigma_i^z - \sigma_j^z) - t (\sigma_i^+ \sigma_j^- + \sigma_i^- \sigma_j^+) \right] \\
&= \frac{1}{4} (\mathbb{1} - \sigma_i^z \sigma_j^z) + \frac{1-t^2}{4(1+t^2)} (\sigma_i^z - \sigma_j^z) - \frac{t}{1+t^2} (\sigma_i^+ \sigma_j^- + \sigma_i^- \sigma_j^+) \\
&\rightarrow \frac{1}{4} (\mathbb{1} - \sigma_i^z \sigma_j^z) + \frac{\eta}{4} (\sigma_i^z - \sigma_j^z) - \frac{\gamma}{2} (\sigma_i^+ \sigma_j^- + \sigma_i^- \sigma_j^+) =: \tilde{P}_{i,j}(\eta, \gamma)
\end{aligned} \tag{A10}$$

The final line is the two-parameter generalization, expressed

as a function of η and γ , that was introduced as Eq. (3).

-
- [1] T. Haseda and A. R. Miedema, “Specific heat of $\text{Cu}(\text{NH}_3)_4\text{SO}_4 \cdot \text{H}_2\text{O}$ below 1 °K,” *Physica* **27**, 1102–1112 (1961).
- [2] R. B. Flippen and S. A. Friedberg, “Low-temperature magnetic susceptibilities of some hydrated formates of Cu^{++} and Mn^{++} ,” *The Journal of Chemical Physics* **38**, 2652–2657 (1963).
- [3] G. R. Wagner and S. A. Friedberg, “Linear chain antiferromagnetism in $\text{Mn}(\text{HCOO})_2 \cdot 2\text{H}_2\text{O}$,” *Physics Letters* **9**, 11–13 (1964).
- [4] Daniel Hone, Claudio Scherer, and Ferdinando Borsa, “Proton spin-lattice relaxation in TMMC $[(\text{CH}_3)_4 \text{NMnCl}_3]$,” *Phys. Rev. B* **9**, 965–974 (1974).
- [5] F. Borsa and M. Mali, “Experimental study of high-temperature spin dynamics in one-dimensional heisenberg paramagnets,” *Physical Review B* **9**, 2215–2219 (1974).
- [6] N. Motoyama, H. Eisaki, and S. Uchida, “Magnetic susceptibility of ideal spin-1/2 Heisenberg antiferromagnetic chain systems, Sr_2CuO_3 and SrCuO_2 ,” *Phys. Rev. Lett.* **76**, 3212–3215 (1996).
- [7] D. Bitko, T. F. Rosenbaum, and G. Aeppli, “Quantum critical behavior for a model magnet,” *Phys. Rev. Lett.* **77**, 940–943 (1996).
- [8] R. Coldea, D. A. Tennant, E. M. Wheeler, E. Wawrzynska, D. Prabhakaran, M. Telling, K. Habicht, P. Smeibidl, and K. Kiefer, “Quantum criticality in an ising chain: Experimental evidence for emergent E8 symmetry,” *Science* **327**, 177–180 (2010).
- [9] Oliver Breunig, Markus Garst, Andreas Klümper, Jens Rohrkamp, Mark M. Turnbull, and Thomas Lorenz, “Quantum criticality in the spin-1/2 Heisenberg chain system copper pyrazine dinitrate,” *Science Advances* **3** (2017), 10.1126/sciadv.aao3773.
- [10] I. A. Zaliznyak, C. Broholm, M. Kibune, M. Nohara, and H. Takagi, “Anisotropic spin freezing in the $S = 1/2$ zigzag chain compound SrCuO_2 ,” *Phys. Rev. Lett.* **83**, 5370–5373 (1999).
- [11] A. Auerbach, *Interacting Electrons and Quantum Magnetism*, Graduate Texts in Contemporary Physics (Springer New York, 2012).
- [12] K. M. Kojima, Y. Fudamoto, M. Larkin, G. M. Luke, J. Mermin, B. Nachumi, Y. J. Uemura, N. Motoyama, H. Eisaki, S. Uchida, K. Yamada, Y. Endoh, S. Hosoya, B. J. Sternlieb, and G. Shirane, “Reduction of ordered moment and Néel temperature of quasi-one-dimensional antiferromagnets Sr_2CuO_3 and Ca_2CuO_3 ,” *Phys. Rev. Lett.* **78**, 1787–1790 (1997).
- [13] R. Bursill, G. A. Gehring, D. J. J. Farnell, J. B. Parkinson, Tao Xiang, and Chen Zeng, “Numerical and approximate analytical results for the frustrated spin-1/2 quantum spin chain,” *Journal of Physics: Condensed Matter* **7**, 8605–8618 (1995).
- [14] R. Jafari and A. Langari, “Phase diagram of the one-dimensional $S = 1/2$ XXZ model with ferromagnetic nearest-neighbor and antiferromagnetic next-nearest-neighbor interactions,” *Phys. Rev. B* **76**, 014412 (2007).
- [15] Keola Wierschem and Pinaki Sengupta, “Characterizing the Haldane phase in quasi-one-dimensional spin-1 Heisenberg antiferromagnets,” *Modern Physics Letters B* **28**, 1430017 (2014).
- [16] Subir Sachdev, *Quantum Phase Transitions* (Cambridge University Press, 2000).
- [17] T. Hirano, H. Katsura, and Y. Hatsugai, “Topological classification of gapped spin chains: Quantized Berry phase as a local order parameter,” *Physical Review B* **77**, 094431 (2008).
- [18] Frank Pollmann, Erez Berg, Ari M. Turner, and Masaki Oshikawa, “Symmetry protection of topological phases in one-dimensional quantum spin systems,” *Physical Review B* **85**, 075125 (2012).
- [19] Elliott Lieb, Theodore Schultz, and Daniel Mattis, “Two soluble models of an antiferromagnetic chain,” *Annals of Physics* **16**, 407–466 (1961).
- [20] Jose I. Latorre, E. Rico, and G. Vidal, “Ground state entanglement in quantum spin chains,” *Quantum Information & Computation* **4**, 48–92 (2004), quant-ph/0304098.
- [21] J. P. Keating and F. Mezzadri, “Entanglement in quantum spin chains, symmetry classes of random matrices, and conformal field theory,” *Physical Review Letters* **94**, 050501 (2005).
- [22] F. D. M. Haldane, “Nonlinear field theory of large-spin Heisenberg antiferromagnets: Semiclassically quantized solitons of the one-dimensional easy-axis Néel state,” *Physical Review Letters* **50**, 1153–1156 (1983).
- [23] F. Duncan M. Haldane, “Nobel lecture: Topological quantum matter,” *Rev. Mod. Phys.* **89**, 040502 (2017).

- [24] Elliott Lieb, Theodore Schultz, and Daniel Mattis, “Two soluble models of an antiferromagnetic chain,” *Annals of Physics* **16**, 407–466 (1961).
- [25] Ian Affleck and F. D. M. Haldane, “Critical theory of quantum spin chains,” *Physical Review B* **36**, 5291–5300 (1987).
- [26] J. Sirker, V. Y. Krivnov, D. V. Dmitriev, A. Herzog, O. Janson, S. Nishimoto, S.-L. Drechsler, and J. Richter, “ J_1 – J_2 Heisenberg model at and close to its $z = 4$ quantum critical point,” *Physical Review B* **84**, 144403 (2011).
- [27] Pranay Patil, Ying Tang, Emanuel Katz, and Anders W. Sandvik, “Indicators of conformal field theory: Entanglement entropy and multiple-point correlators,” *Physical Review B* **96**, 045140 (2017).
- [28] Daichi Hirobe, Masahiro Sato, Takayuki Kawamata, Yuki Shiomi, Ken-ichi Uchida, Ryo Iguchi, Yoji Koike, Sadamichi Maekawa, and Eiji Saitoh, “One-dimensional spinon spin currents,” *Nature Physics* **13**, 30–34 (2017).
- [29] Sougato Bose, “Quantum communication through an unmodulated spin chain,” *Physical Review Letters* **91**, 207901 (2003).
- [30] J. P. Barjaktarevic, R. H. McKenzie, J. Links, and G. J. Milburn, “Measurement-based teleportation along quantum spin chains,” *Physical Review Letters* **95**, 230501 (2005).
- [31] Xingxiang Zhou, Zheng-Wei Zhou, Guang-Can Guo, and Marc J. Feldman, “Quantum computation with untunable couplings,” *Physical Review Letters* **89**, 197903 (2002).
- [32] Stephen D. Bartlett, Gavin K. Brennen, Akimasa Miyake, and Joseph M. Renes, “Quantum computational renormalization in the Haldane phase,” *Physical Review Letters* **105**, 110502 (2010).
- [33] Jonathan Simon, Waseem S. Bakr, Ruichao Ma, M. Eric Tai, Philipp M. Preiss, and Markus Greiner, “Quantum simulation of antiferromagnetic spin chains in an optical lattice,” *Nature* **472**, 307–312 (2011).
- [34] Deung-Jang Choi, Nicolas Lorente, Jens Wiebe, Kirsten von Bergmann, Alexander F. Otte, and Andreas J. Heinrich, “Colloquium: Atomic spin chains on surfaces,” *Rev. Mod. Phys.* **91**, 041001 (2019).
- [35] Ramis Movassagh and Peter W. Shor, “Supercritical entanglement in local systems: Counterexample to the area law for quantum matter,” *Proceedings of the National Academy of Sciences* **113**, 13278–13282 (2016).
- [36] Ramis Movassagh, “The gap of Fredkin quantum spin chain is polynomially small,” *Annals of Mathematical Sciences and Applications* **3**, 531–562 (2018).
- [37] Sergey Bravyi, Libor Caha, Ramis Movassagh, Daniel Nagaj, and Peter W. Shor, “Criticality without frustration for quantum spin-1 chains,” *Phys. Rev. Lett.* **109**, 207202 (2012).
- [38] Ramis Movassagh, “Entanglement and correlation functions of the quantum Motzkin spin-chain,” *Journal of Mathematical Physics* **58**, 031901 (2017).
- [39] L. Dell’Anna, O. Salberger, L. Barbiero, A. Trombettoni, and V. E. Korepin, “Violation of cluster decomposition and absence of light cones in local integer and half-integer spin chains,” *Phys. Rev. B* **94**, 155140 (2016).
- [40] Xiao Chen, Eduardo Fradkin, and William Witczak-Krempa, “Quantum spin chains with multiple dynamics,” *Phys. Rev. B* **96**, 180402 (2017).
- [41] Xiao Chen, Eduardo Fradkin, and William Witczak-Krempa, “Gapless quantum spin chains: multiple dynamics and conformal wavefunctions,” *Journal of Physics A: Mathematical and Theoretical* **50**, 464002 (2017).
- [42] Zhao Zhang, Amr Ahmadain, and Israel Klich, “Novel quantum phase transition from bounded to extensive entanglement,” *Proceedings of the National Academy of Sciences* **114**, 5142–5146 (2017).
- [43] Zhao Zhang and Israel Klich, “Entropy, gap and a multi-parameter deformation of the Fredkin spin chain,” *Journal of Physics A: Mathematical and Theoretical* **50**, 425201 (2017).
- [44] Lionel Levine and Ramis Movassagh, “The gap of the area-weighted Motzkin spin chain is exponentially small,” *Journal of Physics A: Mathematical and Theoretical* **50**, 255302 (2017).
- [45] Takuma Udagawa and Hosho Katsura, “Finite-size gap, magnetization, and entanglement of deformed Fredkin spin chain,” *Journal of Physics A: Mathematical and Theoretical* **50**, 405002 (2017).
- [46] Pramod Padmanabhan, Fumihiko Sugino, and Vladimir Korepin, “Quantum phase transitions and localization in semigroup Fredkin spin chain,” *Quantum Information Processing* **18**, 69 (2019).
- [47] Olof Salberger, Takuma Udagawa, Zhao Zhang, Hosho Katsura, Israel Klich, and Vladimir Korepin, “Deformed Fredkin spin chain with extensive entanglement,” *Journal of Statistical Mechanics: Theory and Experiment* **2017**, 063103 (2017).
- [48] Khagendra Adhikari and K. S. D. Beach, “Deforming the Fredkin spin chain away from its frustration-free point,” *Phys. Rev. B* **99**, 054436 (2019).
- [49] Rafael N. Alexander, Amr Ahmadain, Zhao Zhang, and Israel Klich, “Exact rainbow tensor networks for the colorful Motzkin and Fredkin spin chains,” *Phys. Rev. B* **100**, 214430 (2019).
- [50] Luca Dell’Anna, “Long-distance entanglement in Motzkin and Fredkin spin chains,” *SciPost Phys.* **7**, 53 (2019).
- [51] Fumihiko Sugino and Vladimir Korepin, “Rényi entropy of highly entangled spin chains,” *International Journal of Modern Physics B* **32**, 1850306 (2018).
- [52] Libor Caha and Daniel Nagaj, “The pair-flip model: a very entangled translationally invariant spin chain,” (2018), arXiv:1805.07168.
- [53] Olof Salberger and Vladimir Korepin, “Entangled spin chain,” *Reviews in Mathematical Physics* **29**, 1750031 (2017).
- [54] L. Barbiero, L. Dell’Anna, A. Trombettoni, and V. E. Korepin, “Haldane topological orders in Motzkin spin chains,” *Phys. Rev. B* **96**, 180404 (2017).
- [55] Giovanni Ramírez, Javier Rodríguez-Laguna, and Germán Sierra, “Entanglement over the rainbow,” *Journal of Statistical Mechanics: Theory and Experiment* **2015**, P06002 (2015).
- [56] Aline Ramires, “Frustration can be critical,” *Nature Physics* **15**, 1212–1214 (2019).
- [57] Hengcan Zhao, Jiahao Zhang, Meng Lyu, Sebastian Bachus, Yoshifumi Tokiwa, Philipp Gegenwart, Shuai Zhang, Jinguang Cheng, Yi-feng Yang, Genfu Chen, Yosikazu Isikawa, Qimiao Si, Frank Steglich, and Peijie Sun, “Quantum-critical phase from frustrated magnetism in a strongly correlated metal,” *Nature Physics* **15**, 1261–1266 (2019).
- [58] ITensor Library (version 3.1.1).
- [59] Marius Lemm and Evgeny Mozgunov, “Spectral gaps of frustration-free spin systems with boundary,” *Journal of Mathematical Physics* **60**, 051901 (2019).